SPECTROSCOPIC STUDY OF THE GAS CAP RADIATION INTENSITY FOR SIMULATED MARTIAN ATMOSPHERIC PROBES

By Warren Winovich[1] and Paul A. Croce[2]

Ames Research Center, NASA
Moffett Field, California

INTRODUCTION

A high velocity probe launched into an atmosphere of unknown composition offers a unique opportunity to obtain spectrographic information by close-range examination of the radiating species in the shock-heated gas cap. This information can establish the constituents present, and also can yield relative concentrations of the planetary gas mixture. This knowledge could materially aid in the reduction and interpretation of data from other on-board experiments. Such information would prove vital for planning of future space missions and would materially aid in the design of future manned and unmanned vehicles.

The recent Mariner IV experiments, reference 1, and the earth-based spectroscopic measurements of IR, reference 2, and UV scattering, reference 3, suggest that the Mars atmosphere contains at least 33 percent carbon dioxide. The remaining constituents are postulated to be nitrogen and argon. These latter two have not been detected but are tentatively assigned as constituents on the

[1]Research Scientist
[2]1st Lt., Department of the Army, Military Assignment at Ames

basis of abundancy considerations, reference 4, and postulated geological activity.

Seiff and Reese, reference 5, recently pointed out that instrumented, spherically shaped probes of low ballistic coefficient represent a practical design for a Martian atmosphere probe. Typically, a spherical nose radius of the order of 30 cm can be employed. According to the theoretical predictions of Boobar and Foster, reference 6, and the free-flight-range measurements of James, reference 7, the cyanogen formed in the high-temperature gas cap appears to be one of the promising candidates for spectral examination during entry into the Martin atmosphere.

The planetary space probe is designed to make a steep entry (70°-90°) into the atmosphere. Figure 1 illustrates the convective heat-transfer rate as a function of velocity that one calculates for such an entry into an atmosphere of 46 percent CO_2, 23 percent N_2, and 31 percent A. The entry velocity of 6.7 km/sec is taken to be representative for a 1969 launch. For the steep entry angle contemplated, and for the 30-cm radius spherical nose, maximum convective heating occurs almost simultaneously with maximum radiative heating. If an ablative heat shield is employed, the problem arises as to the effect of radiation from the ablation vapors upon the detection of gas-cap radiation, because it is necessary to measure the gas-cap radiation by looking out from within the model into the stagnation zone. A plasma-tunnel study of gas-cap and

ablation-products radiation in a simulated Martian atmosphere forms the subject matter of the present paper.

TEST FACILITY

A schematic view of the plasma-tunnel facility is shown in figure 2. Details of the facility may be found in reference 8. Briefly, it consists of a DeLaval nozzle having a throat diameter of 1.27 cm and having provisions for sustaining a D.C. electric arc between electrodes in the high pressure plenum chamber on the left and the exit of the supersonic nozzle on the right. The metered gas mixture is introduced into the plenum chamber just downstream of the cathode shroud and is heated by the electrical discharge in the constrictor section. The nozzle exit is 15.2 cm in diameter and the flow exhausts into an evacuated test chamber. The test chamber pressure was maintained at a low value by a steam ejector system such that the free jet was approximately balanced. For these conditions a test body with 45 percent blockage can be employed with steady, uniform flow existing at the stagnation region.

TEST BODY AND INSTRUMENTATION

The test body used for this study is shown in figure 3. It consists of a flat-faced cylindrical nose of 10 cm diameter and a 15-degree conical afterbody. The flat-faced nose has corner

rounding sufficient to match the velocity gradient at the stagnation point with that of a 30-cm radius sphere. This shape was arrived at by trial with a pressure-instrumented model. Interchangeable nose sections of various ablation and heat-sink materials were provided.

The conical afterbody contained the source optics system. The 15-degree displacement of the optical axis with respect to the axis of symmetry was necessary to avoid collecting the high intensity radiation from the arc constrictor. A collimating system incorporating a small aperture limited the region viewed and eliminated the background radiation. Details of the collimated collection-optics system are contained in Appendix A. The 15-cm diameter afterbody expanded the flow to a thin tenuous layer over the short, cylindrical skirt just upstream of the base, which insured that the transmitted radiation consisted primarily of stagnation-point radiation. Tests with the source optics blocked insured that no measurable radiation was received from regions other than the stagnation zone.

Figure 4 compares various parameters calculated for the contemplated full scale entry with those selected for the plasma-tunnel simulation tests. The items of importance for radiation test simulation are the velocity, density, and shock stand-off distance. As shown on the figure, all are matched except the density which is a factor of 30 low. This mismatch in density is equivalent to

an increase in altitude of about 27 km (8 km = scale ht) over the altitude at the peak heating condition. It corresponds to a point in time on the entry trajectory 4 seconds prior to peak radiation heating. Consequently, the test conditions correspond directly to an expected full-scale situation, but not the most severe.

Referring to figure 1 again, the test conditions fall within the stippled area shown on the trajectory curve. For the test conditions, figure 5 illustrates the test body with the radiating gas cap for the case of a non-ablating copper wall.

Instrumentation for the tests is shown in figure 6. The source optics within the test body directs radiation from the gas cap out the rear flange via a first-surface mirror. After passing through the wind tunnel port, the radiation is reflected to a cylindrical first-surface mirror where the circular beam is focused as a line on the entrance slit of a spectrograph. The spectrograph had a focal ratio of 6.8 and was equipped with a 1200 groove/mm grating blazed at 3500 Å. The gas-cap spectra in the range 2700 to 6500 Å were recorded by means of photographs. The plates were calibrated with the model in place by directing a collimated beam from a tungsten ribbon filament lamp into the source optics. The radiative intensity of the tungsten filament was determined by measuring brightness temperature with an optical pyrometer and by recourse to the emissivity data of Larrabee (ref. 9) to obtain a blackbody temperature. Details of the calibra-

tion are given in Appendix B.

The film was Kodak Spectrographic plate film type 103 F. Exposure times for both tests and calibrations were such that the reciprocity law, i.e., $I \times \tau = \text{const.}$, pertains for the photographic emulsion. Photographic densities were read with a Joyce Loebel microdensitometer.

RESULTS AND DISCUSSION

The gas-cap radiation was measured in the arc-jet facility for non-ablating and ablating surfaces. Experimental results for a non-ablating copper surface are shown in figure 7. Total radiation per unit volume is plotted against velocity. The effect of free-stream density is accounted for by using the correlating parameter suggested by theoretical calculations (refs. 10 and 11). The gas mixture consisted of 46 percent CO_2, 23 percent N_2, and 31 percent Argon (percents by volume). The present results are compared with the molecular theory prediction for CO_2-N_2 mixtures of reference 10. The theory has been adjusted to correspond to the same percentages (by volume) as the test gas (i.e., 46 percent CO_2, 23 percent N_2, 31 percent A). This adjustment was made by applying (1) the experimental correlation obtained by James (ref. 7) for concentration effects and (2) the theoretical dilution correlation of reference 10. The ballistic range and shock tube data of references 7, 10, and 12 with no argon dilution

are also shown. The theory of reference 10 agrees well with these results. The present data also show the predicted trend with velocity and agree with the dilution effect of argon predicted by the theory of reference 10. The adjusted theoretical curve which applies to the present gas mixture differs by factors of 2.5 at 5 km/sec to 1.2 at 7 km/sec. Possible explanations for this discrepancy are considered below.

The present data were obtained for values of density ratio sufficiently low to match the contemplated density ratios ($10^{-5} < \rho_\infty/\rho_o < 10^{-3}$) during the time preceeding maximum gas-cap radiation for the Mars probe entry. As noted above, for these low densities the data are only in reasonable agreement with equilibrium theory, whereas the ballistic range and shock tube data which generally agree closely with theory were obtained at sufficiently high density and scale to insure equilibrium.

Nonequilibrium effects in the present results were assessed by assuming that CN forms according to $CO + N \rightleftarrows CN + O$. For this reaction, the CN formation is limited by the concentration of CO. For this chemical model, the relaxation distance for the reaction $CO_2 \rightleftarrows CO + O$ can be found from reference 13. For the present density range ($\rho_\infty/\rho_o = 1 - 5 \times 10^{-5}$) a 50 percent change in the concentration of CO in the stagnation region will occur in a distance of 20 mm, which is approximately equal to the shock stand-off distance. In the plasma tunnel, expansion occurs only to a

Mach number of 6.2. Accordingly, at operating conditions of 13.4 Mj/kg (5.10 km/sec) the free stream is predissociated to a value of z = 1.40 as compared to the equilibrium value at the stagnation state of z = 1.90. On the basis of the free stream predissociation level, the CN concentration behind the bow shock has been estimated to be 87 percent of the equilibrium value. Consequently, the radiation, assuming constant temperature, is predicted to be a factor of 1.2 ($= 0.87^{-1.48}$) below equilibrium values. This factor accounts for the discrepancy at high velocity (6.85 km/sec) but does not completely account for the discrepancy at low velocities.

Although an ablating heat shield would reduce probe launch weight, ablation vapor formation can drastically affect the gas-cap spectra. The radiation characteristics for various heat shield materials were assessed in gas mixtures that consisted of 6 2/3 percent CO_2, 91 percent N_2, and 2 1/3 percent A (by volume). Figure 8 presents spectra of the gas cap for the non-ablating copper nose and for several plastic heat shield materials. The wavelength range of the spectrograms is from 3500 to 6700 Å. For the non-ablating copper surface the radiative flux is due almost solely to the CN violet band system. The three lower spectra are for exactly the same flow conditions but with surfaces of polyethylene, polytetrafluoroethylene, and polyformaldehyde. The gas-cap spectra are quite similar for each of the three plastics.

In addition to enhanced CN violet radiation, the ablation-vapor radiation consists of C_2 Swan band radiation and the C_2 High-Pressure band system. The hydrocarbon plastics also display a prominent CH 4300 Å band series and appreciable hydrogen line radiation. A trace amount of hydrogen appears in the spectrum for the copper surface.

Because the CN violet band system appears to be well understood and amenable to analysis both in terms of species concentration and velocity derived from trajectory data, it represents a prime candidate for monitoring radiation during entry into an atmosphere with CO_2 and N_2 constituents. However, the plasma tunnel tests indicate sizable enhancement of the CN violet system by the presence of ablation ejecta in the boundary layer. The enhancement of the CN violet system by the ablators is shown in Figure 9. Radiation only from the CN violet system is listed relative to the non-ablating copper surface. All of the plastic ablators increased the CN violet band system radiation by approximately the same amount (values range from 3 to 4). These data are apparently contrary to ballistic range and shock tube data which show little or no increase in total radiation with polytetrafluoroethylene and polyformaldehyde models (refs. 7 and 14). In the following discussion ablation measurements from an air study are used to show that there is in fact no inconsistency and that

one can estimate the ablation vapor radiation relative to the gas-cap radiation.

The effect of body radius on the intensity of radiation from an ablating body is illustrated in figure 10. The integrated total intensity over the wavelength range 3600 to 6700 Å is compared for polyethylene models of several radii operated in a plasma tunnel at constant conditions. These tests were performed in air using polyethylene models of the same blunt shape but with smaller radii. The effects of running in air rather than in CO_2-N_2-A mixtures is considered to be unimportant here since only relative changes in the ablation vapor zone radiation were considered. Moreover, the present measurements indicated that the gas-cap radiation forms a relatively small part of the total observed radiation for both flows. Therefore, the scaling law for ablation vapor radiation will depend only weakly on the main flow constituents. Since conditions were constant, the change in radius for this series is equivalent to a change in convective heating rate (ref. 15). The data are shown normalized to the intensity for the smallest model (6.2 mm). The solid line shown represents the predicted scaling law for ablation vapor zone radiation derived in Appendix C (equation C-9). The experimental trend agrees well with the approximate formulation.

flow time is equivalent.

Using the measured enhancement of radiation for ablation of polyethylene (fig. 9), the scaling law for ablation vapor radiation

(equation C-16) and for the gas-cap radiation (fig. 7) can be used to predict the relative intensities for gas-cap radiation as compared to the total radiation received. The approximate scaling law has been applied to typical ballistic range measurements and to the contemplated Mars entry (fig. 1). All comparisons are for a velocity of 5.6 km/sec. The results of such a calculation are shown in figure 11. For the cases illustrated, the contribution of gas-cap radiation is shown. Thus, for plasma tunnel tests with ablation the gas-cap radiation--which would represent the signal one wishes to analyze--is only 1/4 of the total signal. On the other hand, the ballistic range data will contain less than 10 percent contribution from ablation vapors. Plastic models, therefore, can be used in ballistic ranges with negligible uncertainty regarding the radiation source. Finally, for the contemplated full-scale case at peak heating, there is a 20 percent contribution from the ablation vapor zone, while at an earlier time in trajectory (4 seconds prior) there is over a 70 percent contribution. The ablative heat shield would give a signal that contains a variable amount of ablation vapor zone contribution which would introduce uncertainty into the interpretation of the gas-cap constituents for the Mars atmosphere. For this reason, atmospheric probes should probably incorporate heat-sink shields to prevent gas-cap contamination with ablation vapors and thus avoid uncertainties in the interpretation of spectral measurements.

CONCLUDING REMARKS

1. Radiation from CO_2-N_2-A mixtures appears to be well understood. Tests approaching equilibrium conditions in the gas cap agree well with theory (when intensities are normalized with respect to density rather than pressure as pointed out in ref. 11), suggesting that CN violet radiation may be an important tool for probing distant planetary atmospheres with CO_2 and N_2 as constituents.

2. Ablative heat shield materials substantially alter the total radiation. Ablation ejecta can increase the observed intensities of the CN violet system by as much as a factor of 4--depending on the free-stream density at the time of measurement. For this reason, atmospheric probes should probably incorporate heat-sink shields to prevent gas-cap contamination with ablation vapors and thus avoid uncertainties in the interpretation of spectral measurements.

3. Proper scaling of density and body radius (i.e., convective heating rate) is required to simulate radiative intensities for planetary entries where peak heating rates are not high (such as a Mars entry). This is essential in view of the significant contribution to radiation that is possible from the ablation ejecta in the stagnation region. Moreover, nonequilibrium concen-

tration of the molecules at low densities can appreciably alter the emitted radiation.

REFERENCES

1. Kliore, A., Cain, D. L., Levy, G. S., Eshleman, U. R., Fjeldbo, G., and Drake, F. D.: Occultation Experiment: Results of the First Direct Measurements of Mars' Atmosphere and Ionosphere; Science, Vol. 149, No. 3689, September 10, 1965.

2. Kaplan, L. D., Munch, G., Spinrad, H.: Astrophysics Journal, Vol. 139, No. 1 (1964).

3. Evans, D. C.: Ultraviolet Reflectivity of Mars, Science, Vol. 149, No. 3687, August 27, 1965.

4. Menzel, H.: Our Sun, Harvard University Series, 1950.

5. Seiff, A., and Reese, D. E.: Defining Mars' Atmosphere, Astro. and Aero., February 1965.

6. Boobar, M. G., and Foster, R. M.: Some Aerothermodynamic Considerations for Martian Entry and Heat Shield Design, IAS Paper 62-163 (1962).

7. James, C. S.: Experimental Study of Radiative Transport from Hot Gases Simulating in Composition the Atmospheres of Mars and Venus, AIAA Journal, Vol. 2, No. 3, March 1964.

8. Stine, H. A., Watson, V. R., and Shepard, C. E.: Effect of Axial Flow on the Behavior of the Wall-Constricted Arc; Agardograph 84; September 1964.

9. Larrabee, R. D.: Spectral Emissivity of Tungsten, Journal of the Optical Society of America, Vol. 49, No. 6, June 1959.

10. Arnold, J. O., Reis, V. H., and Woodward, H. T.: Studies of Shock-Layer Radiation of Bodies Entering Planetary Atmospheres, AIAA Journal, Vol. 3, No. 11, November 1965.

11. Wolf, F., and Horton, T.: Effect of Argon Addition on Shock-Layer Radiance of CO_2-N_2 Gas Mixtures, AIAA Journal, Vol. 2, No. 8, August 1964.

12. Thomas, G. M., and Menard, W. A.: Total Radiation Heat Transfer Gage for Hypervelocity Shock Tube Experiments, JPL TR No. 32-636, August 1964.

13. Howe, J. T., Viegas, J. R., and Sheaffer, Y. S.: Study of the Nonequilibrium Flow Field Behind Normal Shock Waves in Carbon Dioxide, NASA TN D-1885, June 1963.

14. Steinberg, M., Maiden, C. J., Leak, W. R., and Hansen, C. F.: Preliminary Studies of the Effects of Ablation Contaminants on Radiation, General Motors Defense Res. Lab. Report TR 62-209 H, December 1962.

15. Marvin, J. G., and Deiwert, G. S.: Convective Heat Transfer in Planetary Gases, NASA TR R-224, July 1965.

16. Katzen, E. D., and Kaattari, G. E.: Inviscid Hypersonic Flow Around Blunt Bodies, AIAA Journal, Vol. 3, No. 7, July 1965.

17. Bailey, H. E.: Equilibrium Thermodynamic Properties of Three Engineering Models of the Martian Atmosphere, NASA SP-3021, 1965.

18. Rohsenow, W. M., and Choi, H. Y.: Heat, Mass, and Momentum Transfer, Prentice-Hall, 1961.

19. Rutgers, G. A. W., and DeVos, J. C.: Relation Between Brightness Temperature, True Temperature, and Colour Temperature of Tungsten, Physica XX, 1954.

20. Gruszczynski, J. S., and Warren, W. R.: Experimental Heat-Transfer Studies of Hypervelocity Flight in Planetary Atmospheres, AIAA Journal, Vol. 2, No. 9, September 1964.

21. Boison, J. C., and Curtiss, H. A.: An Experimental Investigation of Blunt Body Stagnation Point Velocity Gradient, ARS Journal, Vol. 29, No. 2, February 1959.

22. Van Dyke, M. D., and Gordon, H. D.: Supersonic Flow Past a Family of Blunt Axisymmetric Bodies, NASA TR R-1, 1959.

23. Craig, R. A., and Davy, W. C.: Thermal Radiation from Ablation Products Injected into a Hypersonic Shock Layer, NASA TN D-1978, September 1963.

ACKNOWLEDGMENT

The authors are deeply indebted to Mr. Walter Stevens for his invaluable assistance in performing these tests.

LIST OF FIGURES

HEATING RATE FOR A SPHERE ENTERING SIMULATED MARS ATMOSPHERE.

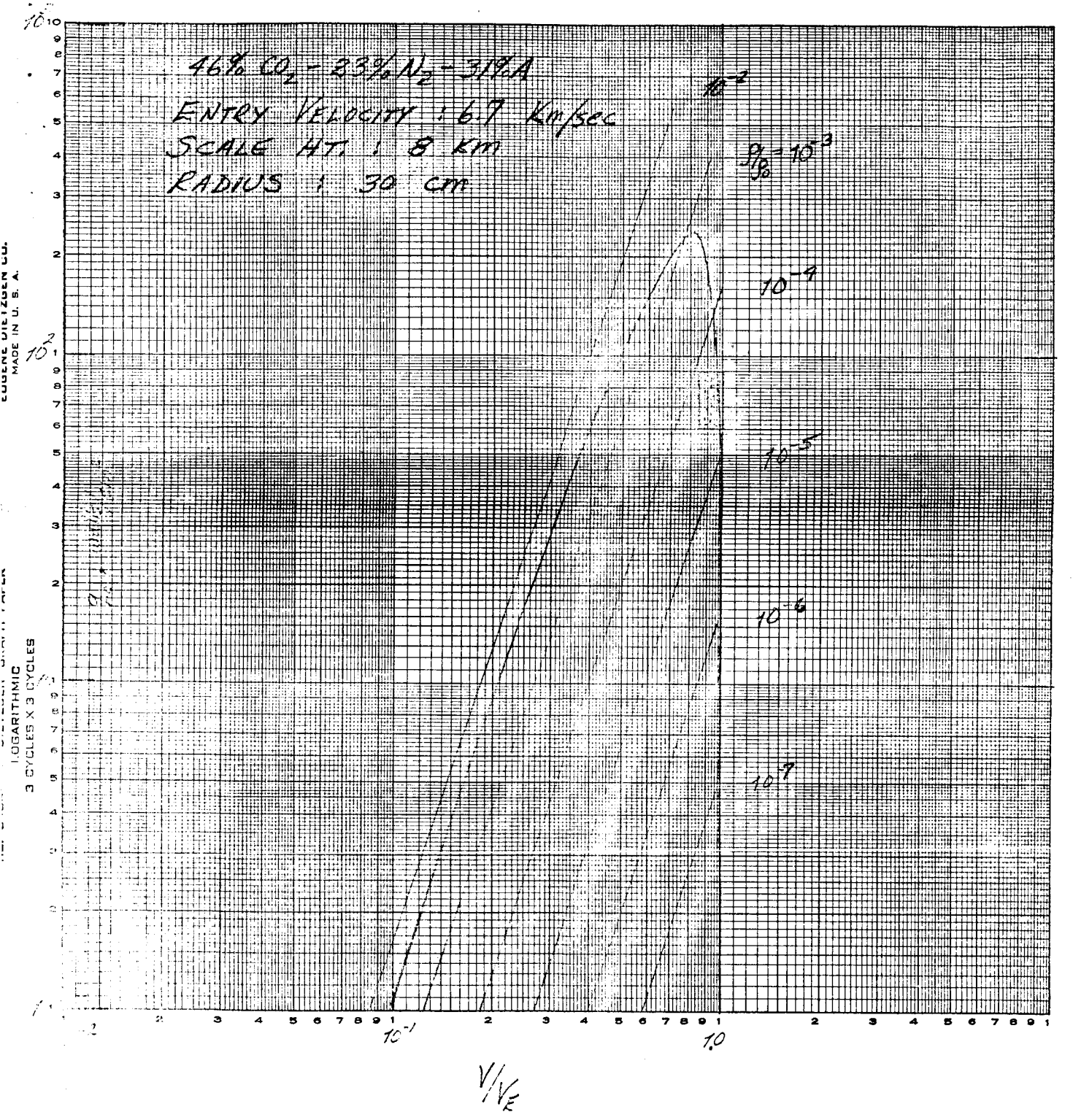

FIG. 1

CONSTRICTED - ARC PLASMA TUNNEL

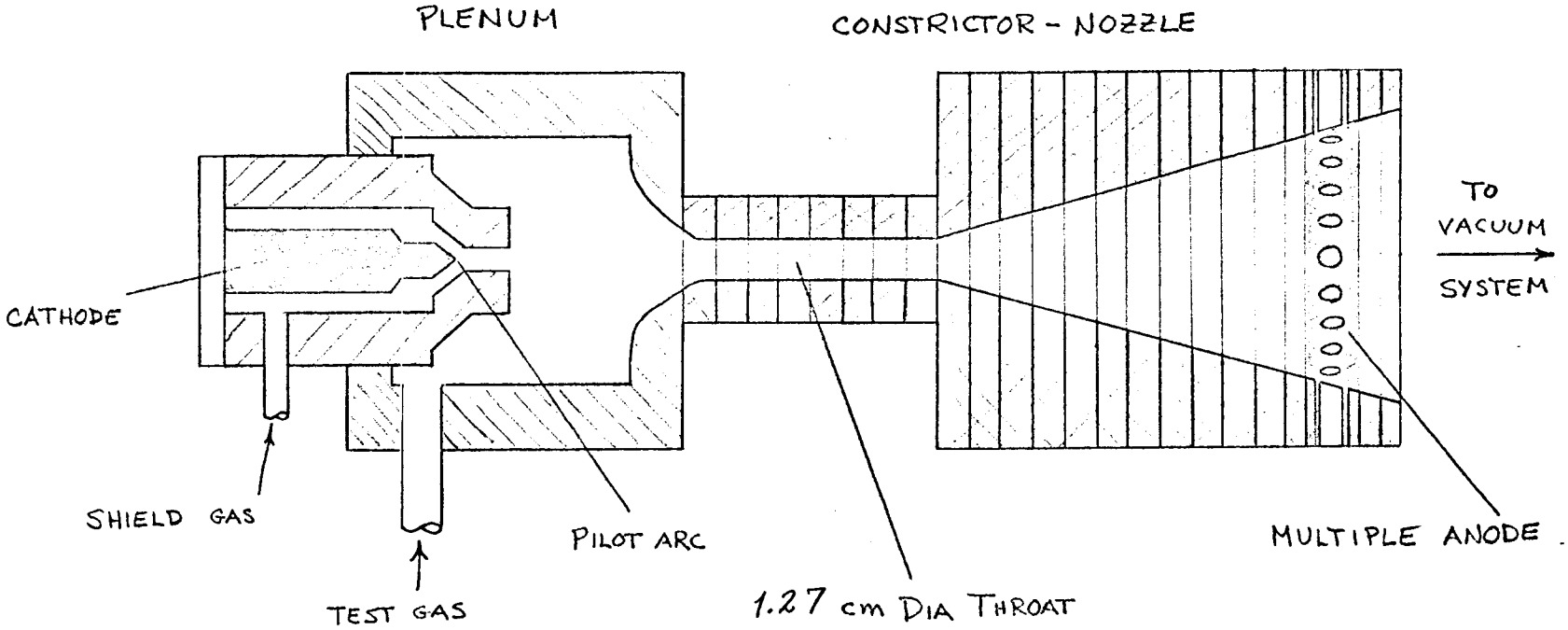

FIG. 2

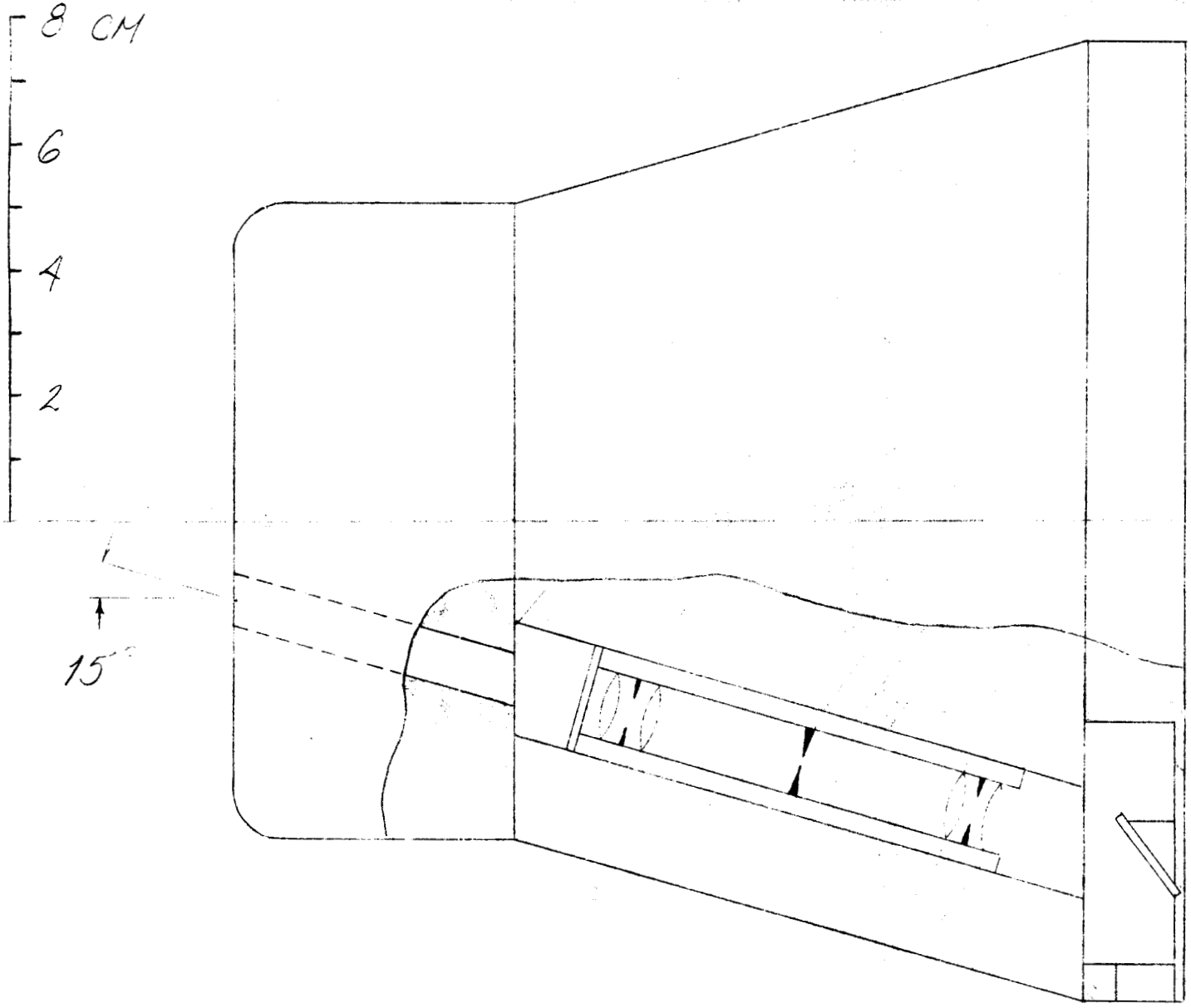
8 см
6
4
2
15°

$V_E = 6.7$ km/sec ; $R = 30$ cm

	Entry Conditions at 76km Altitude	Ground Level
Stag Enthalpy (MJ/kg)	15.7	13.4
V_∞ ($= 0.83 V_E$) (km/sec)	5.6	5.18
Stag Pressure (Atm)	0.15	0.02
ρ_∞/ρ_0	6.7×10^{-4}	2.38×10^{-5}
Shock Stand-off (mm)	20	23
Heating Rate (Watts/cm^2)	246	90
Reynolds Number	30,000	1700
Mach Number	21	6.2

FIG 4

FIGURE 5. GAS CAP RADIATION

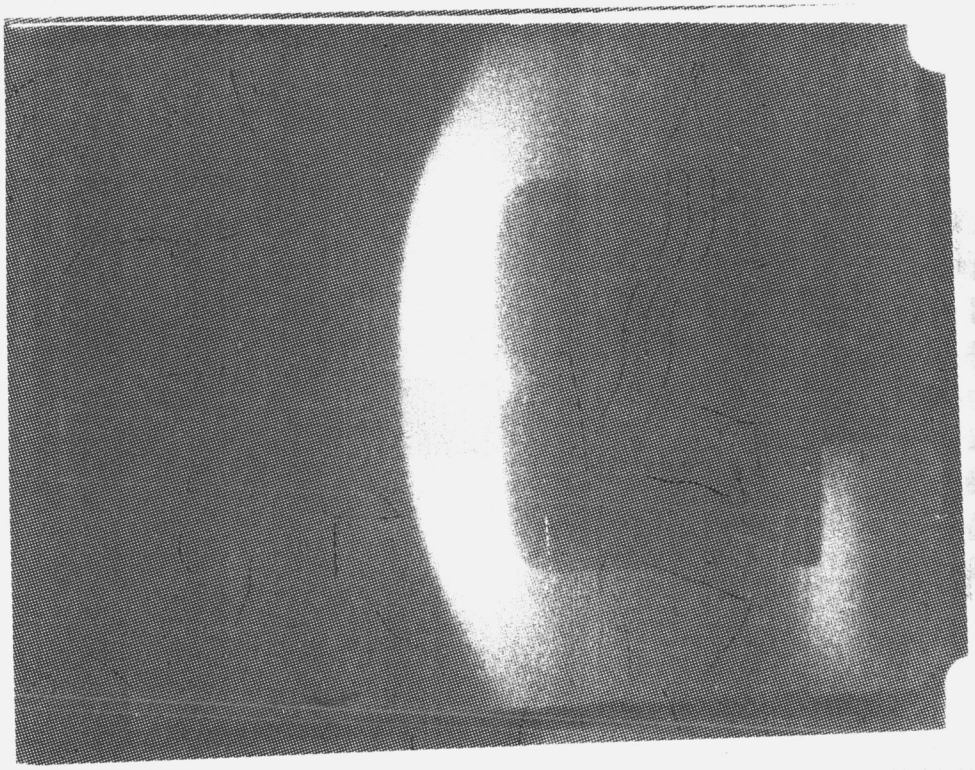

EXPERIMENTAL ARRANGEMENT

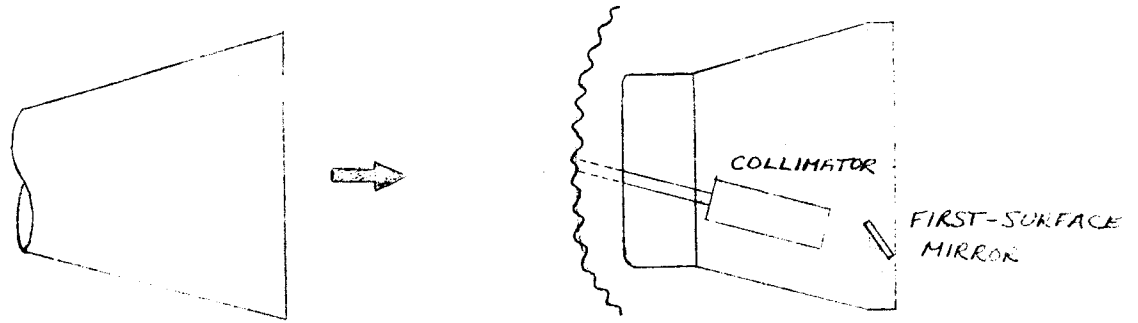

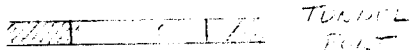

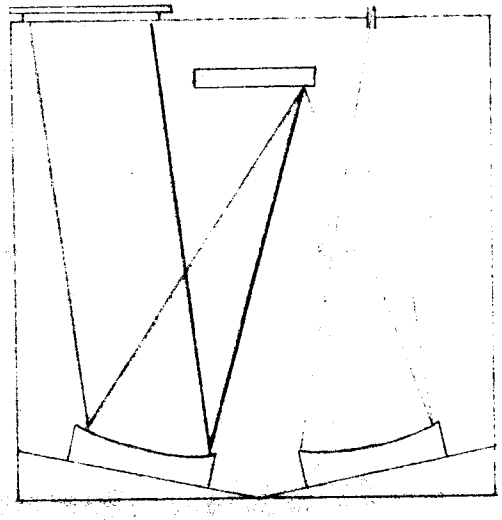

Fig 7.

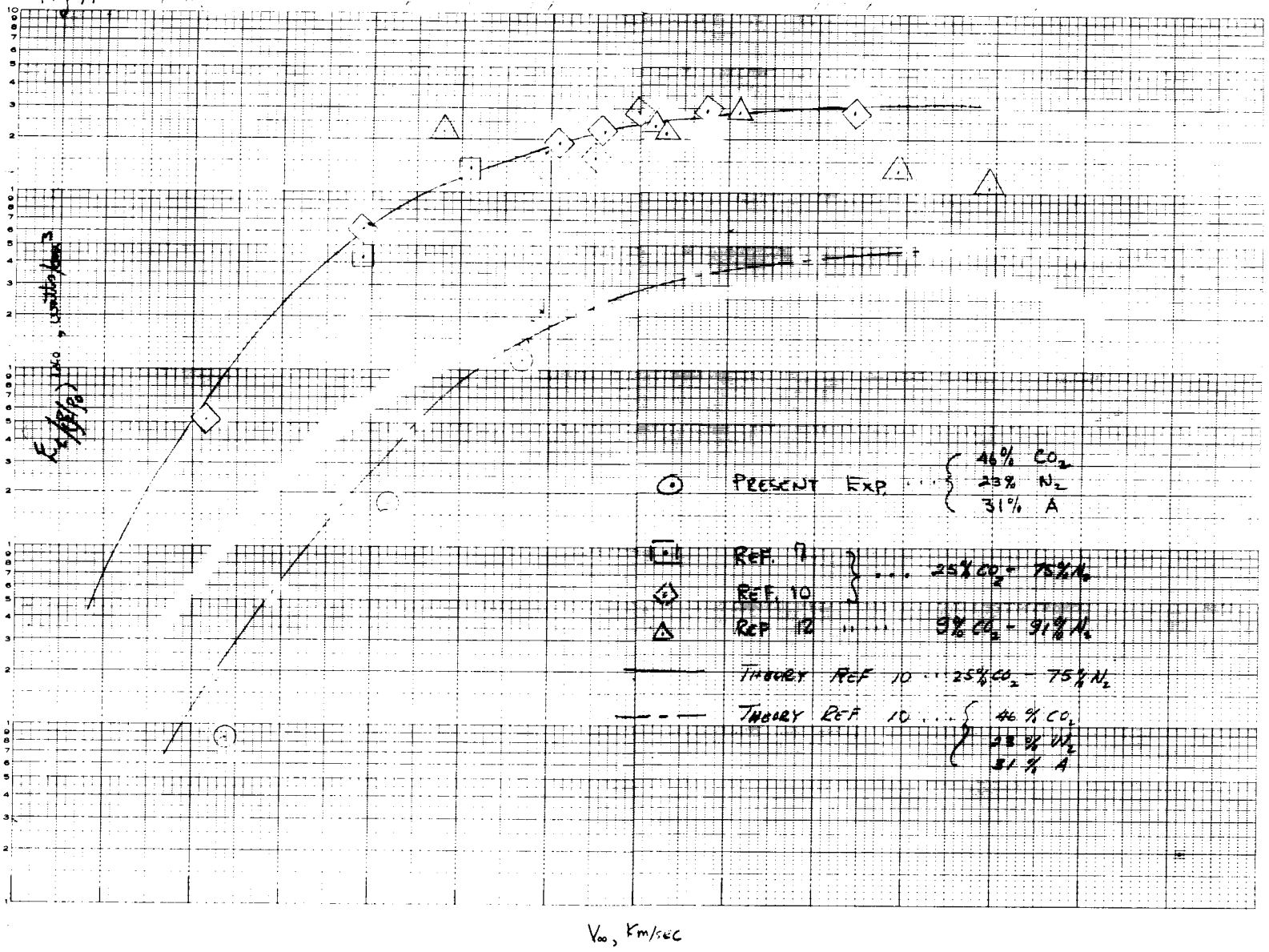

GAS CAP SPECTRA FOR NON-ABLATING AND ABLATING SURFACES

GAS: $6\frac{2}{3}\%\ CO_2 - 91\%\ N_2 - 1\frac{1}{3}\%\ A$; $V_\infty = 8.37$ Km./sec ; $\rho_1/\rho_0 = 1.60 \times 10^{-5}$

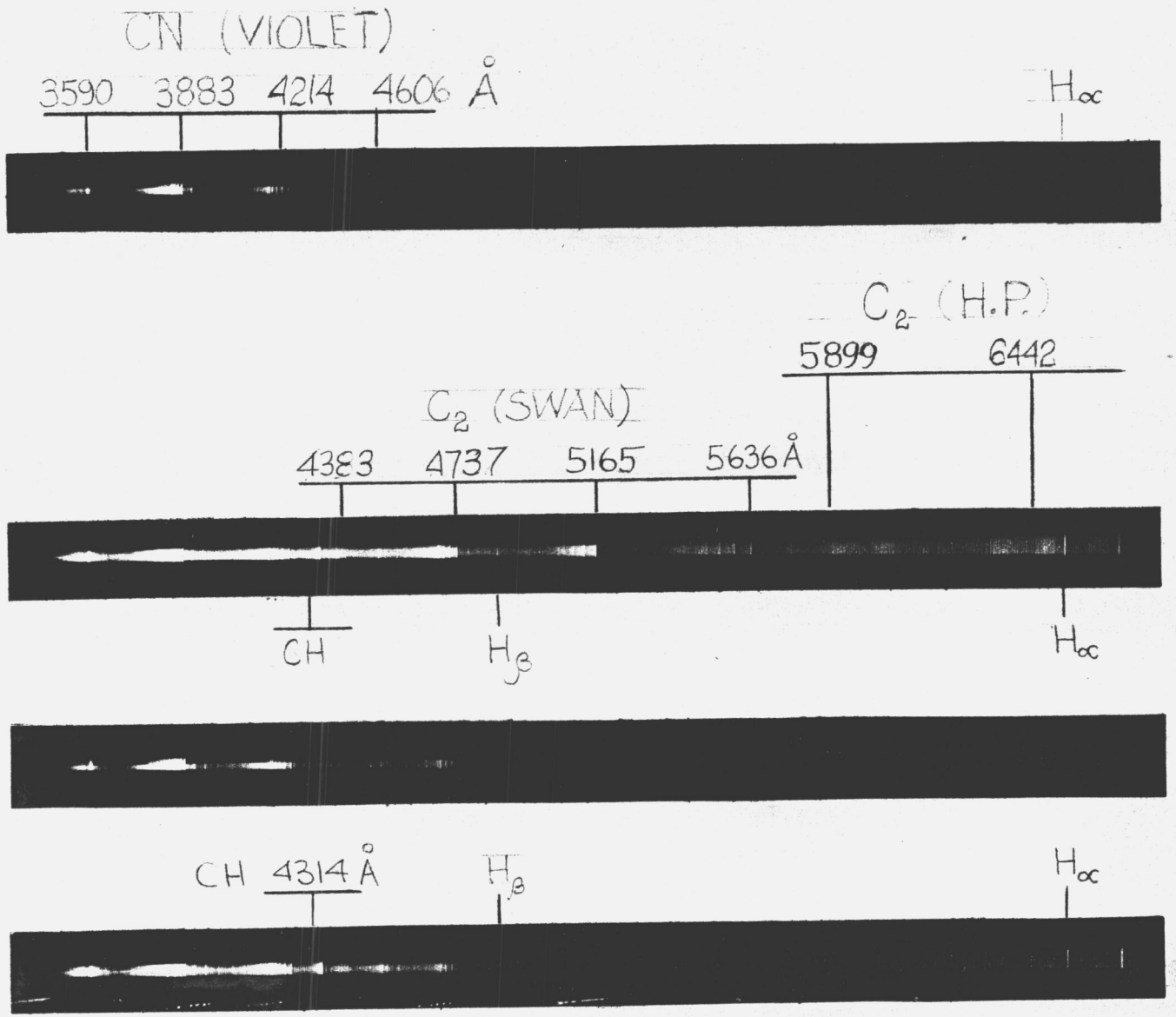

ENHANCEMENT OF CN VIOLET BAND SYSTEM DUE TO ABLATION

$q_{rc} = 170$ watts/cm^2

$h_t = 36$ MJ/Kg (8.5 Km/sec)

SURFACE	NORMALIZED CN BAND INTENSITY
COPPER	1.0
POLYETHYLENE	4.0
POLYTETRAFLUOROETHYLENE	3.3
POLYFORMALDEHYDE	3.0

EFFECT OF BODY RADIUS ON RADIATIVE INTENSITY FOR ABLATING POLYETHYLENE MODELS

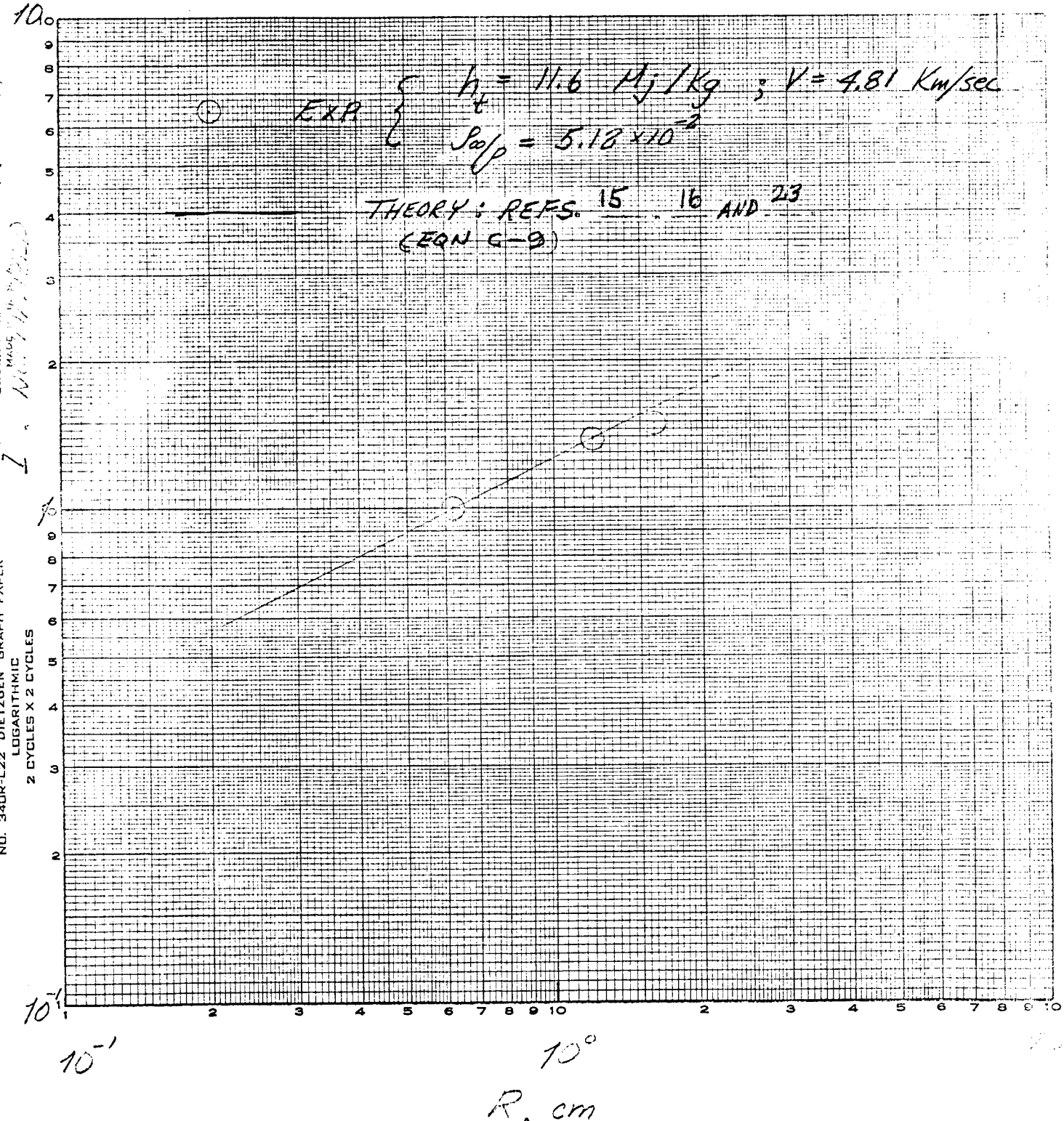

FIG. 10

$V_\infty = 5.6$ km/sec

Case	R_c, cm	ρ_{sea}/15	$\frac{E_{exp}}{E_{exp} + E_{abs}}$
Arc Jet	20	10^{-5}	0.25
Ballistic Range	2	10^{-4}	0.41
Full Scale			
a. Peak Hts.	30	10^{-4}	0.60
b. Peak Hts. – 4 sec	30	10^{-5}	0.27

LIST OF SYMBOLS

A	area (cm^2)
a	radius coordinate (cm)
c	speed of light (cm/sec)
d	$\Delta/\cos 15^\circ$ (App. A)(cm); diameter (App B)(cm)
E	energy (watts)
$[E_{spect}(\lambda)]$	energy metered by spectrograph (watts/μ)
$Eg(\lambda)$	radiation energy density in gas cap (watts/cm^3 μ)
E_t	total radiation energy density in gas cap (watts/cm^3)
e_b	black body function (ergs/cm^2 sec)
F	radiation energy per unit mass (watts/gm)
f	focal length (cm)
H_a	intrinsic heat capacity of ablation material (Mj/kg)
h	distance along optical axis (App. A)(cm); Planck's constant (App. B)(erg sec)
h_t	stagnation enthalpy (Mj/kg)
h_w	wall enthalpy (Mj/kg)
[height at λ]	height of densitometer trace at wavelength
I	radiant intensity (erg/cm^2 sec steradian)
I_t	stagnation point radiation intensity (watts/cm^2)
K	constant in stagnation heating rate formulation (App. C)
k	Boltzmann's constant (erg/$^\circ$K)
l	length (cm)
M	molecular weight (gram/gram-mole)

SYMBOLS - Continued

$\dot{m}$	ablation mass loss rate per unit area (gram/cm^2 sec)
p	pressure (dynes/cm^2)
p_{t_2}	stagnation pressure (dynes/cm^2)
Q	total energy rate (watts)
q_c	convective heating rate (watts/cm^2)
q_{c_o}	convective heating rate with no ablation (watts/cm^2)
R	body radius (cm); surface reflectivity (App. B)
R_c	radius of curvature (cm)
$\bar{R}$	universal gas constant (erg/gm-mole ^{o}K)
r	distance between radiating surfaces (cm)
T	absolute temperature (^{o}K); transmissivity
T_a	wall ablation temperature (^{o}K)
V	velocity (km/sec)
v	volume (cm^3)
z	molecular weight ratio
α	temperature potential parameter
β	ablation constant for material
Δ	shock stand-off distance (cm)
δ	ablation vapor zone thickness (cm)
ϵ	surface emissivity
θ	angle determined by lens optics (App. A); angle coordinate (App. B)
κ	thermal conductivity (watts/cm ^{o}K)

λ	wavelength (cm)
ρ	density (gm/cm^3)
τ	exposure time (sec)
φ	direction angle
Ψ	convective heat blockage ratio

Subscripts

∞	free stream
o	reference conditions (1 earth atmosphere at $288^{\circ}K$)
1	background region (App. A); lens 1 (App. B)
2	region behind normal shock; lens 2 (App. B)
3	lens 3 (App. B)
a	aperture
E	entry
g	ablation vapor gas
M	mirror
T	transmitted beam
s	tungsten source
x	surface x
y	surface y
gas cap	value observed when observing gas cap
calib	value observed when observing tungsten source

Appendix A. Analysis of Collimator for Collection of Gas Cap Radiation.

In the original arrangement for collecting radiant energy a single lens was utilized to view a solid angle of radiating gas, Figure A-1. As is shown on the figure, radiant energy was collected from inside the test body through a small aperture on which the lens was focused. As will be shown, however, background radiation from the arc jet stream ahead of the bow shock wave contributed substantially to the total signal because the observed volume of gas increases as the cube of the distance from the principal focus. Moreover, the high temperatures and pressures that existed upstream in the constrictor of the arc jet provided an additional very intense source. To reduce this background signal, collimation was employed as shown in Figure A-2.

The behavior of the collimation device, Figure A-2, is compared here with that of the system of Figure A-1. To effect a comparison between the two systems, the states of the radiating gas within the respective viewed volumes must be established. For simplicity, temperature and density are assumed to be constant behind the bow shock wave. The free stream conditions were such that the temperature and density ratios across the bow wave were approximately equal to 3.0 and 6.2 respectively. The density ratio was determined from the observed shock standoff distance by using the results of Reference 16, and the pressure ratio was measured during tunnel calibration.

A conservatively low temperature ratio was then obtained from equilibrium charts, Reference 17. The temperature ratio of 3.0 is a result of dissociation which absorbs about 60 percent of the available thermal energy. The assumption is also made that the gas is transparent.

The total amount of radiation collected is proportional to the number of radiators and their radiative strength. Experimental data (Ref. 10) shows that, in the regime of these tests, this quantity can be expressed as

$$Q \propto \rho^{1.4} \, v \, T^4$$

where Q is total radiated energy, ρ is density, v is the volume seen by the collection system, and T is the absolute temperature.

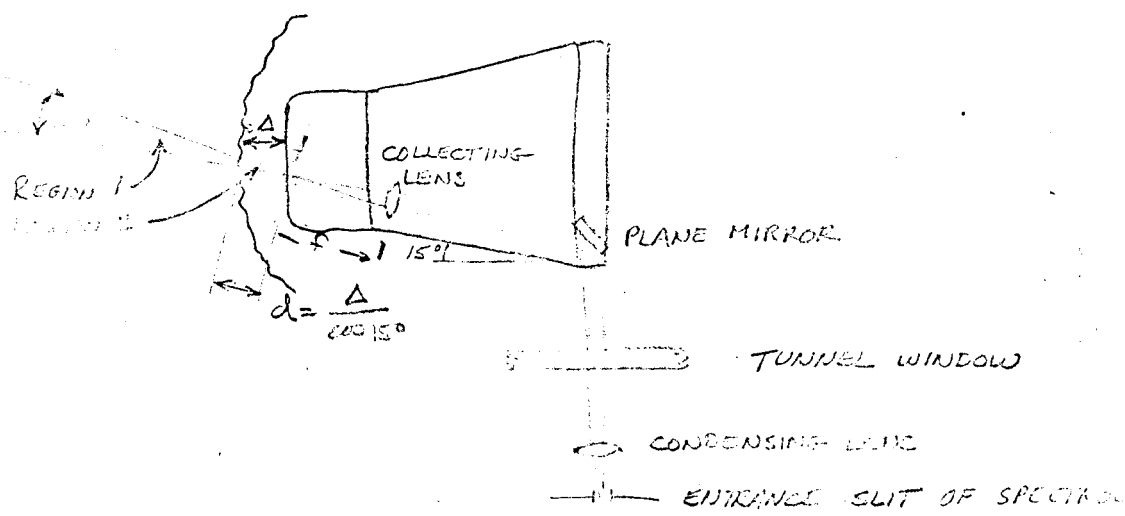

FIGURE A-1

The ratio of gas cap to background radiation, corresponding to radiation from region 1, and region 2 of Figure A-1, can be expressed as

$$\frac{Q_2}{Q_1} = \left(\frac{\rho_2}{\rho_1}\right)^{1.4} \frac{v_2}{v_1} \left(\frac{T_2}{T_1}\right)^4 \qquad \text{(A-1)}$$

where the subscripts refer to the regions indicated on the figure. If h is the distance from the body along the optical axis, and A the corresponding cross-section area of the observed volume, then

$$v_2 = \frac{1}{3} A_2 h_2 = \frac{\pi}{3} d^3 \tan^2 \theta \qquad \text{(A-2)}$$

and

$$v_1 = \frac{1}{3} A_1 h_1 - v_2, \qquad \text{(A-3)}$$

For the present experimental arrangement, $h_1 \cong 15d$, and

$$v_1 = 1125\ \pi d^3 \tan^2 \theta$$

The ratio of gas cap to background radiation therefore becomes

$$\frac{Q_2}{Q_1} = (6.2)^{1.4} \frac{\pi/3\ d^3 \tan^2\theta}{1125\ \pi d^3 \tan^2\theta} (3.0)^4$$

$$= 0.32$$

showing that background radiation can contribute up to 75 percent of the total signal.

For the collimating system shown in Figure A-2, the ratio of gas cap to background radiation can be expressed as

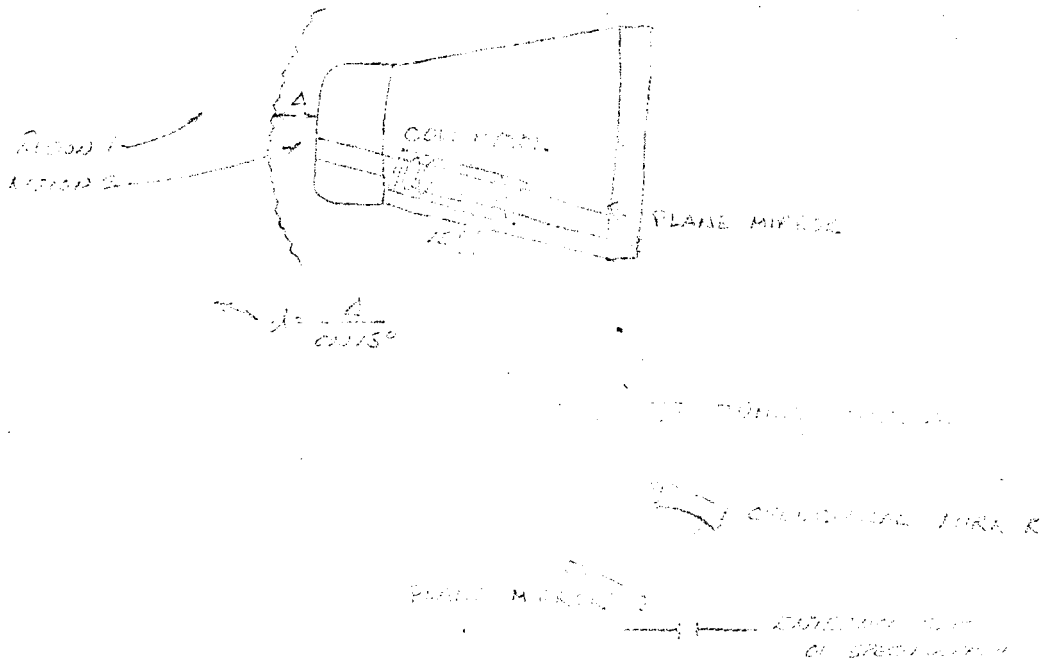

Figure A-2

$$\frac{Q_2}{Q_1} = \left(\frac{\rho_2}{\rho_1}\right)^{1.4} \frac{v_2}{v_1} \left(\frac{T_2}{T_1}\right)^4 .$$

If A is the cross-sectional area of the collimated beam, then

$$v_2 = A\ h_2 = Ad, \text{ and}$$

$$v_1 = A\ h_1 - v_2 \doteq 14\ Ad$$

The radiation ratio therefore becomes

$$\frac{Q_2}{Q_1} = (6.2)^{1.4}\ \frac{Ad}{14\ Ad}\ (3.0)^4$$

$$= 74.4$$

showing that background radiation from the arc-jet stream now represents only slightly more than 1 percent of the total energy received.

In addition to essentially eliminating the signal due to background radiation, the collimator also collected more gas cap radiation than the conventional system. For a given lens diameter, the gas cap signals from the two systems can be compared directly. Again using the fact that $Q \propto \rho^{1.4} v T^4$ and using previous nomenclature, it follows that

$$\frac{(Q_2)_{\text{collimator}}}{(Q_2)_{\text{conventional}}} = \frac{\rho_2^{1.4}(Ad)\ T_2^4}{\rho_2^{1.4}(\pi/3\ d^3 \tan^2\theta)T_2^4} \qquad \text{(A-4)}$$

$$= \frac{3A}{\pi d^2 \tan^2\theta}$$

For the preliminary work, $d \cong 26$ mm, $\theta \cong 4^\circ$, $A \cong 50$ mm^2. Substituting these values into the above expression yields

$$\frac{(Q_2)_{\text{coll}}}{(Q_2)_{\text{conv}}} = \frac{(3)(50)}{\pi(26.4)^2(0.00487)} = 14$$

Although a conventional system utilizing a very high f-number lens will yield similar results, for a usable signal in the present tests an impractically long focal length would be required.

Appendix B. Calibration for Absolute Intensity

To calibrate for absolute intensities, energy radiated from a tungsten ribbon filament lamp was collimated, passed through the source collection system (see Appendix A), and focused on the slit of the spectrograph with the test body in place. Figure B-1 shows the arrangement for calibration.

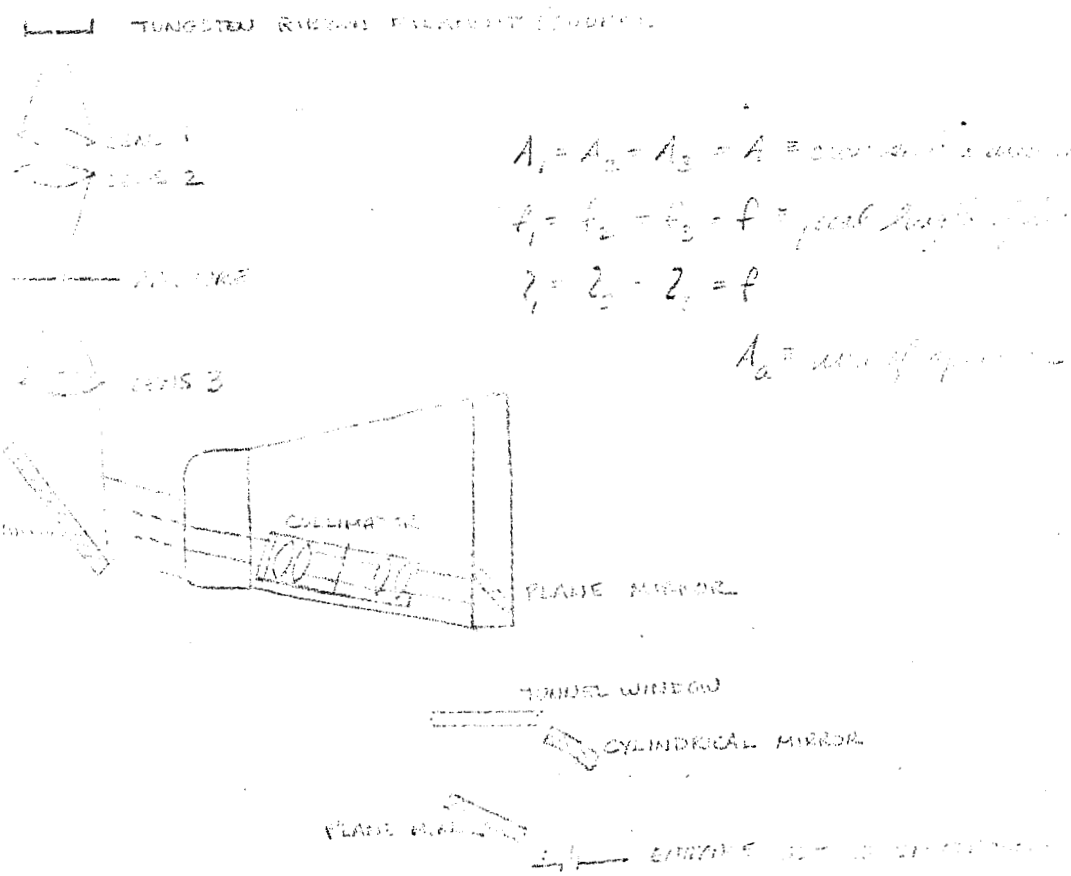

Figure B-1

The basic relation for radiant energy transfer between two surfaces is given in reference 18 as

$$d^2E_{x-y} = I \frac{dA_x \cos \varphi_x \, dA_y \cos \varphi_y}{r^2} \qquad \text{(B-1)}$$

where E_{x-y} is the energy (watts) leaving the elemental area dA_x, and arriving at the elemental area dA_y, I is the constant radiant intensity (watts/cm^2 steradian) between dA_x and dA_y, r is the distance (cm) between dA_x and dA_y and φ_x and φ_y are the angles between r and the normals of dA_x and dA_y respectively. (See Figure B-2.)

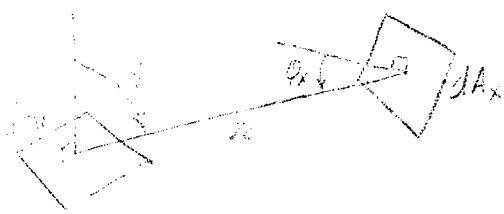

Figure B-2.

Integrating over A_x and A_y,

$$E_{x-y} = I \int_{A_x} \int_{A_y} \frac{\cos \varphi_x \cos \varphi_y}{r^2} \, dA_x \, dA_y \qquad \text{(B-2)}$$

For a gray surface with large grey surroundings, $I = \epsilon_x e_{b_x}/\pi$ where ϵ_x is the emissivity of surface x, e_{b_x} is the black body function of surface x, and for $T_y \ll T_x$

$$E_{net} \quad E_{x-y} - E_{y-x}$$

$$= E_{x-y} = \frac{\epsilon_x e_{b_x}}{\pi} \int_{A_x} \int_{A_y} \frac{\cos \varphi_x \cos \varphi_y}{r^2} \, dA_x \, dA_y \qquad (B\text{-}3)$$

Applying this relation to the calibration technique with subscript s for the tungsten source and subscript 1 for lens 1, we have

$$E_{s-1} = \frac{\epsilon_s e_{bs}}{\pi} \int_{A_s} \int_{A_1} \frac{\cos \varphi_s \cos \varphi_1}{r^2} \, dA_s \, dA_1 \qquad (B\text{-}4)$$

Making the usual thin lens approximation that lens 1 be considered a plane, it follows that A_1 is parallel to A_s so that $\varphi_s = \varphi_1 = \varphi$. Also, since only the energy passing through the aperture A_a is used, then only the energy emanating from this area projected back onto the filament enters the system; and since $l_1 = l_2 = f$, the substitution that $A_s = A_a$ can be made. Referring to Figure B-3, we see that, since the aperture diameter, d_a, (= 0.54 mm) << the lens diameter, d_1, (= 22.1 mm),

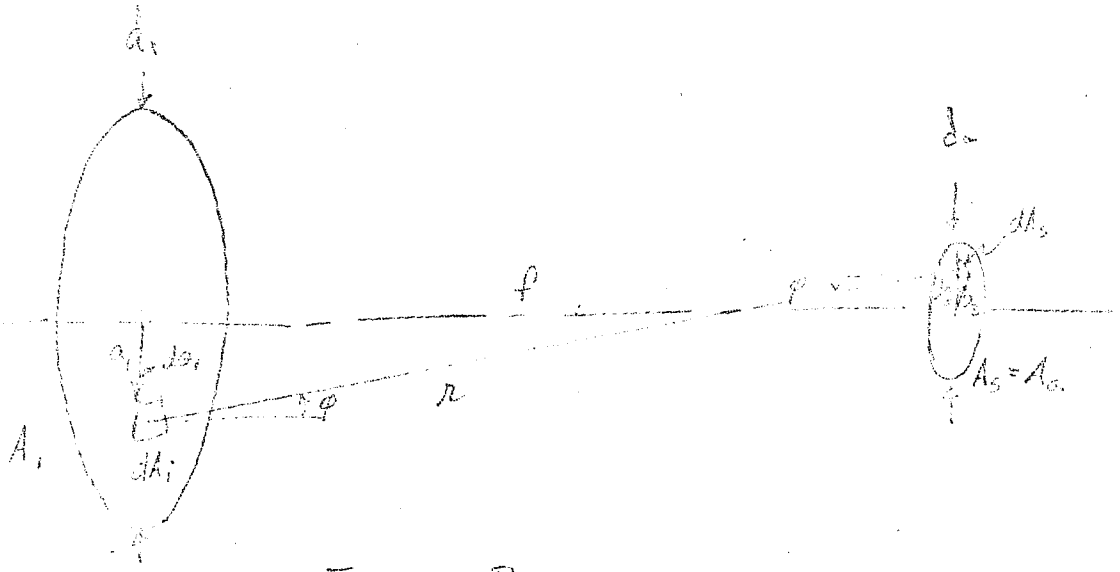

FIGURE B-3

$r^2 = a_1^2 + f_1^2$. It follows that, since $\cos\varphi = f/r$, $\cos^2\varphi = f_1^2/(a_1^2 + f_1^2)$. Since $dA_1 = a_1 da_1 d\theta_1$ and $dA_s = a_s da_s d\theta_s$, we now have

$$E_{s-1} = \frac{\epsilon_s e_{bs}}{\pi} \int_{a_s=0}^{d_a/2} \int_{\theta_s=0}^{2\pi} \int_{a_1=0}^{d_1/2} \int_{\theta_1=0}^{2\pi} \frac{f_1^2}{(f_1^2 + a_1^2)^2} a_s da_s d\theta_s a_1 da_1 d\theta_1 \qquad (B\text{-}5)$$

$$= \frac{\pi}{4} \frac{d_a^2 d_1^2}{4f_1^2 + d_1^2} \epsilon_s e_{bs} \qquad (B\text{-}6)$$

Since the emissivity is wavelength dependent, i.e., $\epsilon_s = \epsilon_s(\lambda)$, we have finally

$$\frac{dE_{s-1}(\lambda)}{d\lambda} = \frac{\pi}{4} \frac{d_a^2 d_1^2}{4f_1^2 + d_1^2} \epsilon_s(\lambda) \frac{2\pi h c^2 \lambda^{-5}}{e^{\frac{hc}{\lambda k T_s}} - 1} \quad \left(\frac{\text{erg}}{\text{sec cm}}\right) \qquad (B\text{-}7)$$

where $h = 6.624 \times 10^{-27}$ erg sec, $c = 3 \times 10^{10}$ cm/sec, $k = 1.38 \times 10^{-16}$ erg/$^\circ$K, λ = wavelength in cm, and T_s = filament temperature in degrees Kelvin.

Since all of the reflection and absorption losses during a test run were present during the calibration, we need only correct for losses in the lens and mirror used to collimate the energy from the tungsten filament and direct it into the model, and for the difference in area between the incident beam and the transmitted (through the model) beam. Letting T be the transmissivity of a lens, R the reflectivity of a mirror, d_T the diameter of the transmitted beam, $\left[E_{spect}(\lambda)\right]$ the energy metered by the spectrograph in $d\lambda$, we have

$$\left[E_{spect}(\lambda)\right] = T_1T_2T_3R_M \frac{d_T}{d_1} \frac{d\left[\epsilon_{s-1}(\lambda)\right]}{d\lambda} \times 10^{-3} \left(\frac{watt}{\mu}\right) \qquad (B-8)$$

For our calibration procedure, $T_1T_2T_3 = 0.653$ (measured using a 4000 Å filter with a half width of 300 Å), $R_M = 0.880$ (measured using same filter), $d_T = 0.506$ cm, $d_1 = 2.21$ cm, $d_g = 0.0540$ cm, and $f_1 = 0.36$ cm, so that

$$\left[E_{spect}(\lambda)\right] = 9.48(10)^{-10} \frac{\epsilon_s(\lambda) 2\, hc^2\lambda^{-5}}{e^{\frac{hc}{\lambda k T_s}} - 1} \left(\frac{watts}{\mu}\right) \qquad (B-9)$$

T_s was determined by measuring the brightness temperature of the tungsten ribbon source with a filament-type optical pyrometer and correcting to the true temperature (ref. 19).

The calibration energy was related to the gas cap energy by directly comparing the heights of densitometer traces and exposure times, τ, of the obtained spectrographic plates, i.e.

$$\frac{\left[E_{spect}(\lambda)\right]_{gas\ cap}}{\left[E_{spect}(\lambda)\right]_{calib}} = \frac{\left[\text{height at } \lambda\right]_{gas\ cap}}{\left[\text{height at } \lambda\right]_{calib}} \cdot \frac{\tau_{gas\ cap}}{\tau_{calib}} \qquad (B-10)$$

The radiation energy density in the gas cap, Eg (λ), was then determined by dividing the measured energy by the effective volume of gas seen by the detector optics as in reference 20. For the present case, energy was collected from a constant property stagnation region so that the effective volume reduces to the actual observed volume. The value for actual observed volume was determined to be 0.481 cm^3 and was used to reduce all measurements. Thus,

$$E_g(\lambda) = 1.981(10)^{-9} \frac{\left[\text{height at } \lambda\right]_{\text{gas cap}}}{\left[\text{height at } \lambda\right]_{\text{calib}}} \cdot \frac{\tau_{\text{gas cap}}}{\tau_{\text{calib}}} \frac{\epsilon_s(\lambda) 2\pi hc^2 \lambda^{-5}}{e^{\frac{hc}{\lambda k T_s}} - 1} \left(\frac{\text{watt/cm}}{\mu}\right)$$

(B-11)

Finally, total energy density was obtained by plotting equation (B-11) versus wavelength and integrating over λ.

Appendix C. Radiation From Ablation Vapor Zone

The derivation given below is an approximate analysis of the scaling relation that pertains to radiation from the ablation vapor zone. The analysis is for laminar flow at the stagnation region of a hemisphere. However, it should apply equally well to blunt bodies since these shapes can be characterized as spheres in terms of an equivalent radius of curvature (ref. 21). For blunt bodies with sharp corners, for example, the equivalent radius of curvature is from 3.5 to 4 times the body radius. The analysis pertains to a subliming ablator.

Gases either injected (ref. 16) or simply ablated into the stagnation region from material degradation form a distinct zone separated from the stagnation flow region by an interface. The thickness of this zone can be obtained from reference 16. Thus,

$$\frac{\delta}{R_c} = \frac{\dot{m}}{\rho_\infty V_\infty} \cdot \frac{\Delta}{R_c} \cdot \sqrt{\frac{\rho_2}{\rho_\infty}} \cdot \sqrt{\frac{\rho_2}{\rho_g}} \qquad \text{(C-1)}$$

For an ablative heat shield, the "effective heat of ablation" relates the convective heating rate and the mass ejecta rate to flow conditions and material properties. For subliming ablators this relation is

$$\frac{q_{co}}{\dot{m}} = H_a + \beta(h_t - h_w) \qquad \text{(C-2)}$$

where H_a is the intrinsic heat capacity of the material and the constant β depends on the molecular weights of the injecta and oncoming flow. For laminar flow at the stagnation point of a

hemisphere, the convective heating rate formulation appearing above is given by (ref. 15) as

$$q_{co} = K\sqrt{\frac{p_{t_2}}{R_c}}\ (h_t - h_w) \qquad (C\text{-}3)$$

Combining equations C-1, C-2, and C-3 and solving for the ablation vapor zone thickness yields

$$\frac{\delta}{R_c} = \frac{1}{\sqrt{R_c}\sqrt{\rho_g}} \left\{ \frac{K}{\beta\left[1 + \frac{H_a}{\beta(h_t - h_w)}\right]} \cdot \frac{\Delta/R_c}{(\rho_\infty/\rho_2)} \right\} \qquad (C\text{-}4)$$

However, for hemispheres, the shock stand-off distance can be approximated over wide density ranges by the simple relation (c.f. ref. 22)

$$\Delta/R_c = 1/(\rho_2/\rho_\infty) \qquad (C\text{-}5)$$

Therefore, the term in equation C-4 within the braces is dependent only on the stagnation enthalpy (or equivalent free-stream velocity). Note that for many common ablation materials the factor $H_a/\beta(h_t - h_w)$ is of the order 0.4 for $V_\infty \geq 5$ km/sec. Consequently, the term within the braces is virtually independent of flow conditions and depends primarily on the ablation gas ejecta. Thus,

$$\delta/R_c = K^1/\sqrt{R_c\ \rho_g} \qquad (C\text{-}6)$$

where the definition of K^1 is given by equation C-4. This last expression indicates that for small scale and/or high density, the thickness of the ablation vapor zone is reduced.

In reference 23 it is shown that for unit mass of ablation products the radiation can be characterized by

$$F = K_2 \rho_g^{\xi} T^{\xi} \tag{C-7}$$

where K_2 is a constant of the material. The radiation intensity at the stagnation point can be written as

$$I = E_t \delta = F \rho_g \delta = K_2 \rho_g^{1+\xi} T^{\xi} \delta \tag{C-8}$$

Combining equation C-8 with equation C-6 and normalizing with respect to the density term, one obtains a scaling relation for intensity:

$$\frac{I}{(\rho_g/\rho_o)^{1/2+\xi}} \propto T_g^{\xi} \sqrt{R_c} \tag{C-9}$$

The temperature of the ablation vapor at the interface is the controlling parameter according to equation C-9 since ξ is typically about 3 (ref. 23). Accordingly, a consideration of the dependence of T_g on flow conditions is in order.

By approximating the ablation vapor zone by a conducting fluid layer, one can write a heat balance at the interface between the ablation vapor zone and the stagnation gas region

$$\Psi q_{co} = \kappa (T_g/T_a)/\delta \tag{C-10}$$

the factor Ψ is the heat blockage ratio defined as

$$\Psi = q_c/q_{co} = H_a/[H_a + \beta(h_t - h_w)] \tag{C-11}$$

for subliming ablators. The effect of diffusion between the stagnation zone and the ablation layer zone is contained in the ablation

ejecta parameter, β. Solving for the ablation vapor gas temperature from equations C-3, C-10, and C-11, one obtains after some algebraic manipulation (and using the usual hypersonic approximation $p_2 \approx p_{t_2}$):

$$T_g/T_a = \alpha/2 + \sqrt{1 + (\alpha/2)^2}$$

where (C-12)

$$\alpha = \frac{K K^1 H_a}{\kappa \sqrt{T_a} \sqrt{R/M_g}} \left\{ \frac{(h_t - h_w)/H_a}{1 + \beta(h_t - h_w)/H_a} \right\}$$

Expanding with the binomial theorem

$$T_g/T_a = 1 + \alpha/2 + 1/2(\alpha/2)^2 \cdots \quad \text{(C-13)}$$

One can verify that for low temperature ablators (polyethylene, for example) only the first two terms are significant in the expansion. Consequently, to good approximation

$$T_g/T_a \approx 1 + \alpha/2 \quad \text{(C-14)}$$

where α is given in equation (C-12).

Referring to the expression for α, note that for a normalized enthalpy potential [$= (h_t - h_w)/H_a$] of about 8 (i.e., $h_t > 12$ Mj/kg or $V_\infty > 5$ km/sec) the term within the braces is within about 20 percent of the limiting value ($= 1/\beta$) for usual plastic ablators. It follows, then, that the temperature of the ablation vapor is relatively insensitive to the incident flow conditions.

Returning to the scaling law formulation for the ablation vapor radiative intensity (equation C-9), one obtains an approximate

result that holds over wide conditions of incident flow ($V_\infty > 5$ km/sec). Namely,

$$\frac{I}{(\rho_g/\rho_o)^{1/2 + \xi}} \propto R_c \text{ , approximately} \qquad (C\text{-}15)$$

Finally, using the relations of equation C-8, the radiation per unit volume is given by

$$\frac{E_t}{(\rho_g/\rho_o)^{1 + \xi}} = \text{constant} \qquad (C\text{-}16)$$

As noted above (equation C-14), the ablation vapor temperature is relatively insensitive to flow conditions over wide limits. Therefore, the ablation vapor radiation per unit volume varies primarily as the ablation vapor gas density raised to some power dependent only on the material. Values of ξ are given in reference 23 for some typical ablation materials. For example, for polyethylene $\xi = 2/3$.